Steel and Composite Structures, *Vol. 27, No. 2 (2018) 161-175*
DOI: https://doi.org/10.12989/scs.2018.27.2.161

In-situ test and dynamic response of a double-deck tied-arch bridge

Hongye Gou [*1,2,3], Wen Zhou [1], Genda Chen [3], Yi Bao [3] and Qianhui Pu [1]

[1] *Department of Bridge Engineering, School of Civil Engineering, Southwest Jiaotong University, Chengdu 610031, China*
[2] *Key Laboratory of High-Speed Railway Engineering, Ministry of Education, Southwest Jiaotong University, Chengdu 610031, China*
[3] *Department of Civil, Architectural, and Environmental Engineering, Missouri University of Science and Technology, Rolla, MO 65401, USA*

(*Received September 30, 2017, Revised January 21, 2018, Accepted February 21, 2018*)

Abstract. In this study, in-situ dynamic tests of the world's longest steel box tied-arch bridge over the Yangtze River, China, are reported. The double deck bridge supports highway and monorail systems at upper and lower levels, respectively. Strain, displacement, and acceleration responses were measured and used to investigate the vibration characteristics of the bridge when excited by running trains and/or trucks at a speed of 5-60 km/h, train braking, and truck bouncing. Impact factors were correlated with the running speed of trains and trucks. A three-dimensional finite element model of the coupled monorail-train-bridge vibration system accounting for track irregularities was established to understand the system behavior and validated by the experimental results. Truck bouncing was the dominant impact factor on bridge responses. The running speed of vehicles determined the riding comfort of traveling trains.

Keywords: straddle-type monorail; double-deck tied-arch bridge; in-situ dynamic test; finite element analysis; vibration; impact; riding comfort

1. Introduction

Due to increasing traffic congestion in urban transportation, monorail systems have recently attracted more attentions worldwide (Lee *et al*. 2005). In a monorail system, the wheels of a train firmly grasp the track of a railway. On one hand, the strong connection between the train and its supporting track makes monorail systems more stable than urban subway systems in operation. On the other hand, the strong connection results in coupled dynamic vibrations of the train, track, and bridge in monorail systems, making the design and analysis of such systems more complicated. Due to the comfort of train riders and the safety of bridge, train and riders, investigation on the dynamic behavior of coupled train-bridge vibration systems is of critical significance.

As more monorail systems are developed and constructed in recent years, a few studies have been reported to understand the dynamic responses of monorail bridges (Goda *et al*. 2000, Lee *et al*. 2006). A computational model was established to analyze the dynamic responses of a coupled train and bridge system (Goda *et al*. 2000). In this model, the train was considered to be rigid including the traverse and rotating degrees of freedom (DOFs). In another study (Lee *et al*. 2006), a train model with 15 DOFs was proposed to describe the behaviors of vertical settlement, nodding, head shaking, side-rolling, and yawing. Most of the reported studies, if not all, are based on numerical simulations that require assumptions and idealizations of the bridge and trains. The computational models may not represent the realistic conditions of a complex bridge-train system particularly in the presence of both railway and highway supported by a double-deck bridge. They have not been validated by experimental results. Model test and In-situ test have been considered as the effective approach to investigate the mechanical performance of bridge structures (Gou *et al*. 2017, 2018a, b). Understanding of the vibrational responses and behaviors of double-deck tied-arch bridges under moving trains and/or trucks is quite limited.

On the other hands, the dynamic responses of train-bridge systems in railways have been extensively investigated under moving trains. Specifically, a 27-m-long, three-span, precast concrete bridge was tested in-situ (Hogan *et al*. 2016). A new class of spread slab beam bridges were developed based on field tests (Jiang *et al*. 2016, Terzioglu *et al*. 2016). The dynamic responses of a 77-year-old single-span steel truss railway bridge were determined from field measurements, modal analysis, and a generalized single DOF analysis (Shibeshi and Roth 2016). The performance of one of the oldest masonry arch bridges in Iran Railway Network was assessed through field tests (Ataei *et al*. 2016). The dynamic responses of a short-span soil-steel composite bridge were analyzed based on limited strain, displacement, and acceleration measurements in the steel and backfill soils (Mellat *et al*. 2014). Yang *et al*. (2015) studied the creep performance of the concrete-filled steel tubular bridge. The seismic performance of railway and highway bridges were analyzed by experimental and numerical methods (Altunisik and Kalkan 2016, Deng *et al*. 2016, Toydemir *et al*. 2017). In the numerical analysis, the effects of impact loads (Xia *et al*. 2012) and track irregularity (Youcef *et al*. 2013) on the dynamic behaviors

*Corresponding author, Ph.D., Associate Professor,
E-mail: gouhongye@swjtu.cn

ISSN: 1229-9367 (Print), 1598-6233 (Online)

of coupled train-bridge systems were evaluated to ensure the safety and riding comfort of high-speed trains (Xia *et al*. 2012). The interaction between wheels of the moving train and track laid on the bridge was taken into account (Dinh *et al*. 2009). The dynamic responses of long-span suspension bridges (Cavdar 2013, Gűnaydin *et al*. 2014, Kwon *et al*. 2008), cable-stayed bridges (Jorquera-Lucerga *et al*. 2016, Madrazo-Aguirre *et al*. 2015) and arch bridge (Gou *et al*. 2018c, d) under running trains have also been studied extensively.

The main objective of this study is to investigate the dynamic behavior and characteristics of the world's longest steel box tied-arch bridge spanning over the Yangtze River in Chongqing City, a double-deck structure supporting both railway and highway. Field tests were carried out under moving trains and trucks with dynamic strains, displacements, and accelerations. Based on the measured strain and displacement, impact factors were investigated and correlated with the running speeds of trains and trucks. A three-dimensional finite element model of the bridge was established and validated by selected experimental results, taking into account the monorail-train-bridge coupling effect and track irregularity. Numerical analyses were performed to understand the dynamic behaviors and interpret the experimental results of the coupled system. Sperling index was used to evaluate the riding comfort level of trains. The experimental data obtained in this study not only ensure the safe operation of the bridge and the riding comfort of passengers, but also provide a reference for future design and research of similar bridges.

2. Description of the bridge

The Caiyuanba Yangtze River Bridge was completed in 2007 and located in Chongqing, China. The main bridge is 800 m long and composed of five spans with a layout of 88 + 102 + 420 + 102 + 88 m, as indicated in Fig. 1(a). It is the longest steel box tied-arch bridge in the world. The main arch has a rise-to-span ratio of 1/5.7. The arch has rectangular cross sections, as shown in Fig. 1(b). A continuous steel truss girder is supported on the arch through 38 suspensors. The cross section of steel girder at mid span is 11.20 m tall, 39.80 m wide at the top, and 13.00 m at the bottom. The steel girder and main arch are fixed on Y-shaped piers. The steel girder is used to support double decks for highway vehicles at the upper level and for trains on monorail track at the low level, as depicted in Figs. 1(c) and (d). The upper deck in a total width of about 30.50 m consists of six 3.75 m wide lanes and two 2.50 m wide walkways. The designed driving speed of trucks at the upper level is 60 km/h. The lower deck supports a double-line, straddle-type monorail. The designed running speed of trains is 75 km/h.

3. In-situ Experimental Program

3.1 Test plan

Ambient vibration tests and vehicle loading tests were carried out on the Caiyuanba Yangtze River Bridge.

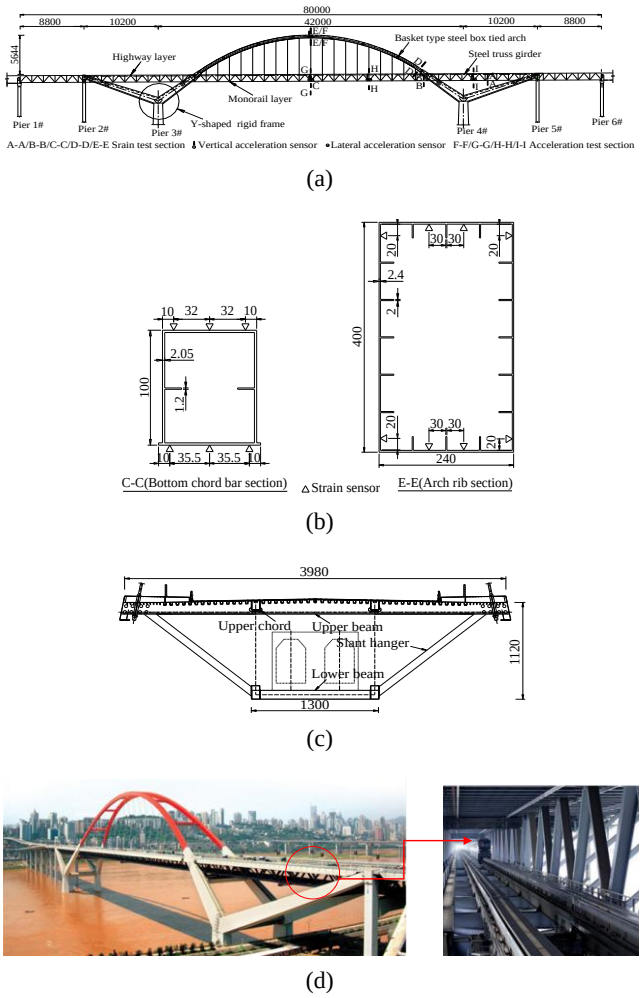

Fig. 1 The Caiyuanba Yangtze River Bridge (unit: cm): (a) elevation view; (b) cross section of bottom chord (C-C) and arch rib at mid span (E-E); (c) cross section of steel truss girder at mid span (G-G); (d) overview

Ambient vibration tests were conducted to generate free vibration and investigate the natural frequencies, mode shapes, and damping ratio of the bridge. Truck and train loading tests were conducted in different scenarios to generate force vibration and investigate the dynamic responses, impact effect, and comfort index of the bridge. The loading scenarios included: (1) moving truck test at various speeds; (2) truck impact test; (3) moving train test in one way or two ways; (4) train braking test; and (5) combined moving truck and train test.

The moving truck tests were conducted with two trucks that traveled in the same direction along the centerline of lanes at a constant speed of 5, 10, 20, 30, 40, 50, and 60 km/h, respectively. The truck impact tests were carried out with one truck moving along the centerline of the upper deck at a speed of 5, 10, 15, 20, 25, and 30 km/h, respectively. At each speed, the moving truck passed over a 7.5 cm high triangular obstacle, which applied an impact load on the bridge deck, simulating the effect of local damage in pavement on bridge responses. The dynamic responses of the bridge structure were measured to evaluate

impact factors that are applicable to the bridge design.

The moving train tests were conducted with one monorail train or two trains in opposite directions traveling through the lower deck of the bridge at a speed of 5, 10, 20, 30, 40, 50, and 60 km/h, respectively. For train braking tests, one monorail train traveled over the bridge at a speed of 20, 30, and 40 km/h, respectively. The train was braked as it traveled to a critical cross section (mid-section in the middle span) of the bridge, resulting in the most unfavorable loading effect. The critical cross section was determined through finite element analysis as introduced latter. The dynamic responses of the bridge structure were measured under moving train loads and train braking effects. The comfort index of trains was determined.

For a combined effect of moving truck and moving train, two parallel trucks traveled in the same directions and two parallel trains travelled in the opposite directions at a speed of 5, 10, 20, 30, 40, 50, and 60 km/h, respectively. The two trucks and two trains simultaneously passed through the bridge. The bridge responses measured under moving train and truck loads are used to evaluate the comfort index of trains.

Ambient vibration acceleration of the bridge under wind and water flow effects was measured without any moving vehicles on the two bridge decks. Based on the measured acceleration time domain signal, the spectrum diagram was obtained by fast Fourier transform (FFT) analysis, and the frequencies of the bridge were extracted using peak detection method (Androus *et al*. 2017). ITD time domain modal parameter identification method (Kashani and Nobari 2012) was adopted for vibration mode analysis. Free vibration differential equations for the **N** DOFs viscous damping system can be expressed as

$$\boldsymbol{M}\ddot{\boldsymbol{X}} + \boldsymbol{C}\dot{\boldsymbol{X}} + \boldsymbol{K}\boldsymbol{X} = 0 \tag{1}$$

where $\boldsymbol{M}$, $\boldsymbol{C}$, $\boldsymbol{K}$ are the damping, mass, and stiffness matrices of the bridge, respectively; $\boldsymbol{X}$ is the displacement matric.

The equation of state of the system

$$\begin{vmatrix} \dot{\boldsymbol{X}} \\ \ddot{\boldsymbol{X}} \end{vmatrix} = \begin{vmatrix} 0 & \boldsymbol{I} \\ -\boldsymbol{M}^{-1}\boldsymbol{K} & -\boldsymbol{M}^{-1}\boldsymbol{C} \end{vmatrix} \begin{vmatrix} \boldsymbol{X} \\ \dot{\boldsymbol{X}} \end{vmatrix} \tag{2}$$

The state coefficient matrix

$$\boldsymbol{A} = \begin{vmatrix} 0 & \boldsymbol{I} \\ -\boldsymbol{M}^{-1}\boldsymbol{K} & -\boldsymbol{M}^{-1}\boldsymbol{C} \end{vmatrix} \tag{3}$$

According to the complex mode theory, the system corresponding to the Eq. (1) has 2**N** conjugate complex

(a) Test scenario

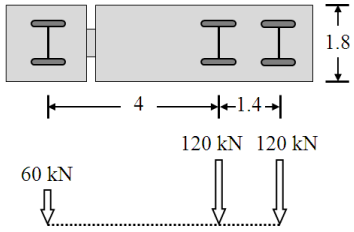

(b) Load distribution of the truck

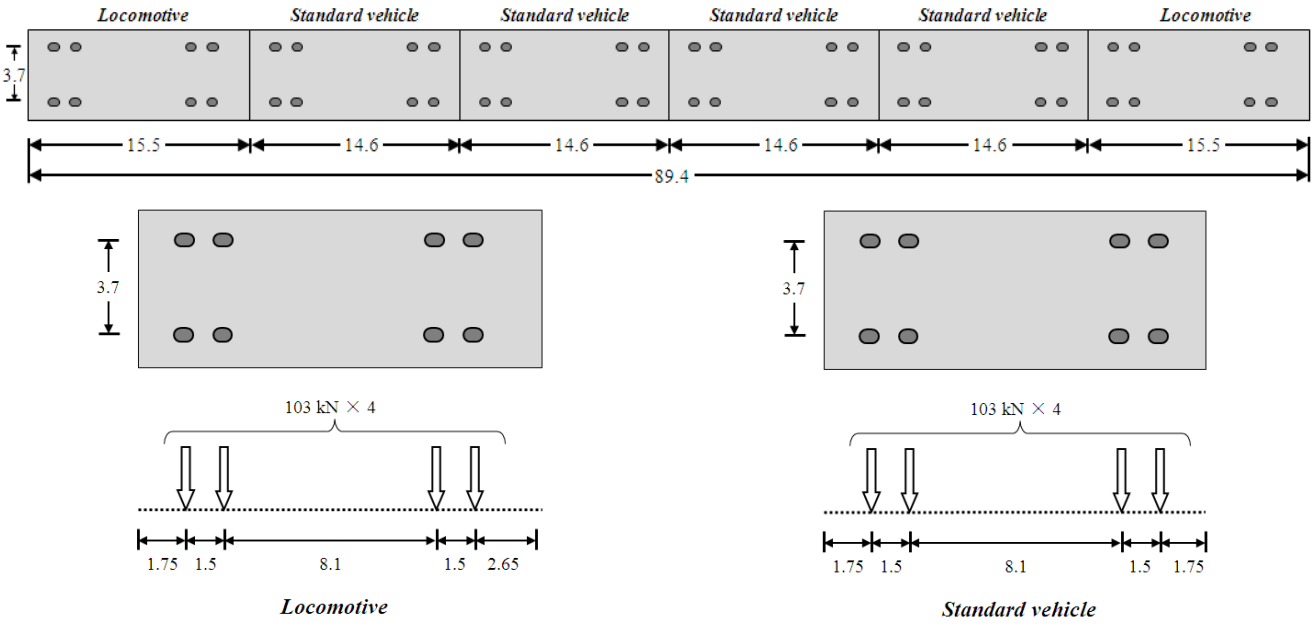

(c) Load distribution of the monorail train

Fig. 2 Axle load and wheelbase distribution diagrams of the loading trucks and trains (unit: m)

eigenvalues $\lambda_i = a_i + jb_i$ and corresponding complex eigenvectors φ_i (i = 1, 2,…, 2N). φ_i is the i_{th} order mode; λ_i is the i_{th} order frequency. The free response $X(t)$ of the system can be written as linear overlapping of the modal responses of each order

$$\boldsymbol{X(t)} = \sum_{i=1}^{2N} \boldsymbol{\varphi_i e^{\lambda_i t}} \tag{4}$$

It can be seen that the response signal of the system contains all modal information. According to the response signal $X(t)$, the state coefficient matrix A of the system was determined. Then, the eigenvalues of the state coefficient matrix were solved, and all the modal parameters of the system were obtained.

3.2 Instrumentation of the bridge

In order to understand the dynamic characteristics and evaluate the performance of the bridge, several critical sections of steel truss girders and arch ribs were instrumented. As shown in Fig. 1(a), 34 electrical resistance strain gauges were deployed at the bottom chords of steel truss girders in the middle of side span (Section A-A), at the location of hangers (Section B-B), and in the middle of mid span (Section C-C), respectively, at the end of arches immediately above the girders (Section D-D), and at the vault section (E-E). As shown in Fig. 1(c), another three strain gauges were installed on the top and bottom faces of the bottom chord of the steel truss girder, respectively. Another two strain gauges were on the roof top and bottom edges, respectively, and four strain gauges on the web plate of the arch rib section.

As shown in Fig. 1(a), four linear variable differential transformers (LVDTs) and four accelerometers were installed at the vault section (F-F), at the middle section of mid span (G-G), at the quarter section of mid span (H-H), and at the middle section of the Y-shaped rigid frame (I-I). The data sampling rate was set to 100 Hz in the data acquisition system.

3.3 Vehicles

The trucks used during loading tests are shown in Fig. 2(a). Fig. 2(b) illustrates the distribution of the axle loads of a truck. The truck weighed 300 kN in total with the front and two rear axis loads of 60, 120, and 120 kN, respectively.

The monorail train used for tests consisted of two head vehicles at two ends and four standard vehicles in between, as depicted in Fig. 2(c). The length of each head vehicle was 15.5 m, while that of each standard vehicle was 14.6 m. Each of the head vehicles and standard vehicles was composed of a vehicle body and two bogies, which were supported on four 103 kN axles.

4. Experimental results and discussion

4.1 Vibration characteristics of the bridge

Based on the measured bridge accelerations in vertical and transverse directions in the ambient vibration tests, the 1st mode shapes of the bridge in the two directions were obtained as shown in Figs. 3(a) and (b), respectively. Specifically, the Fourier spectra of the measured bridge accelerations are presented in Fig. 4. The 1st mode of vibration corresponds to a frequency (F) of 0.660 Hz in the vertical direction, and 0.310 Hz in the transverse direction. The damping ratio (D) was determined from the half-power spectrum bandwidth by Eq. (5)

$$D_n = (f'_{n2} - f'_{n1}) / 2 f_n \tag{5}$$

where f_n denotes the n^{th} frequency; and f'_{n1} and f'_{n2} denote two frequencies at the n^{th} half-power bandwidth. The damping ratio was determined to be 0.020 in the vertical direction, and 0.047 in the transverse direction.

The vibration modes of the bridge based on the numerical model are showed in Fig. 5. The natural frequencies identified from the measured accelerations are summarized in Table 1. In general, the natural frequencies are well spaced for the tested bridge. The vibration modes corresponding to the listed frequencies are also described in Table 1. However, there are still some differences between the measured frequency and the calculated frequency, which may be caused by the following reasons: when the model is established to calculate the natural frequency, the structure is simplified, which is different from the actual structure. The stiffness of some joints is released to some extent when the finite element model is established. The accuracy of the stiffness release has an effect on the calculated frequency. In addition, the simulation of support conditions in the finite

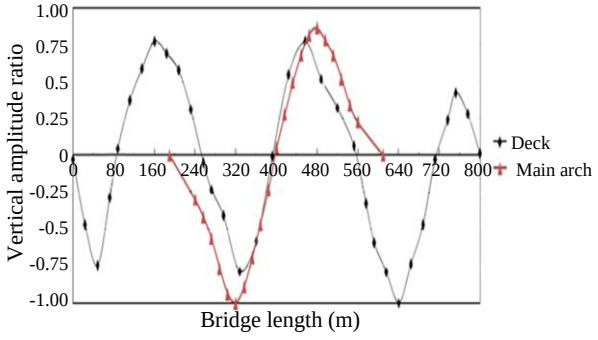

(a) Vertical direction

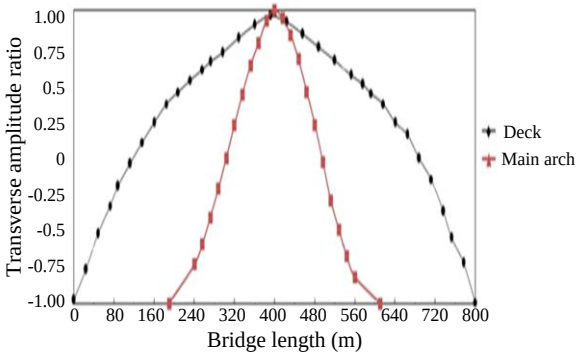

(b) Transverse direction

Fig. 3 The 1st mode shapes of the bridge

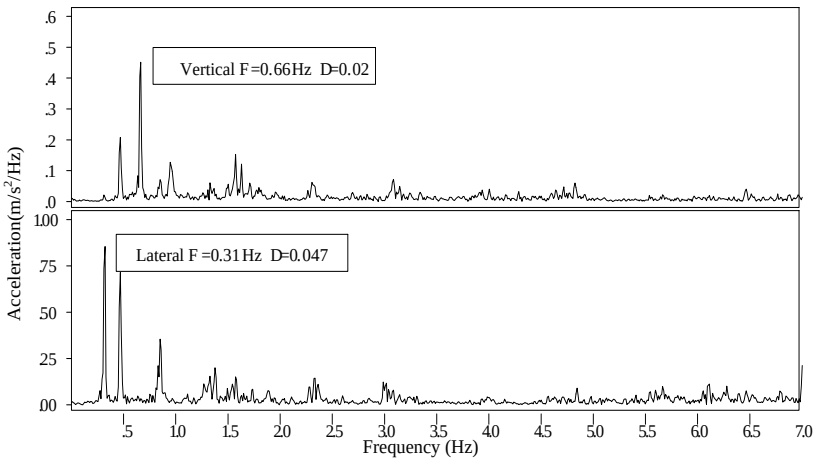

Fig. 4 Fourier spectra of the measured accelerations in vertical and transverse directions

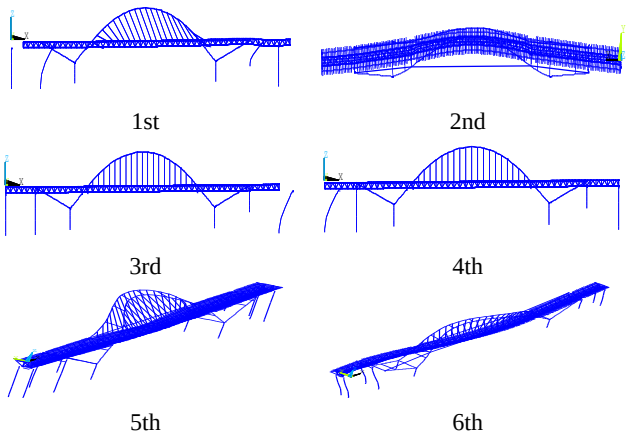

Fig. 5 The numerical vibration modes of the bridge

Table 1 Experimental and numerical results of natural frequencies

Mode No.	Experimental (Hz)	Numerical (Hz)	Error (%)	Description of vibration mode
1	0.310	0.317	2.3	Transverse motion of bridge superstructure
2	0.375	0.388	3.5	Longitudinal motion of bridge girder
3	0.406	0.419	3.2	Transverse motion of bridge girder
4	0.502	0.515	2.6	Transverse motion of steel box tied arch
5	0.531	0.537	1.3	Vertical motion of steel box tied arch
6	0.596	0.609	2.2	Vertical motion of bridge girder

element model will also affect the vibration frequency of the structure.

4.2 Impact factor

Impact factor was employed to describe the dynamic

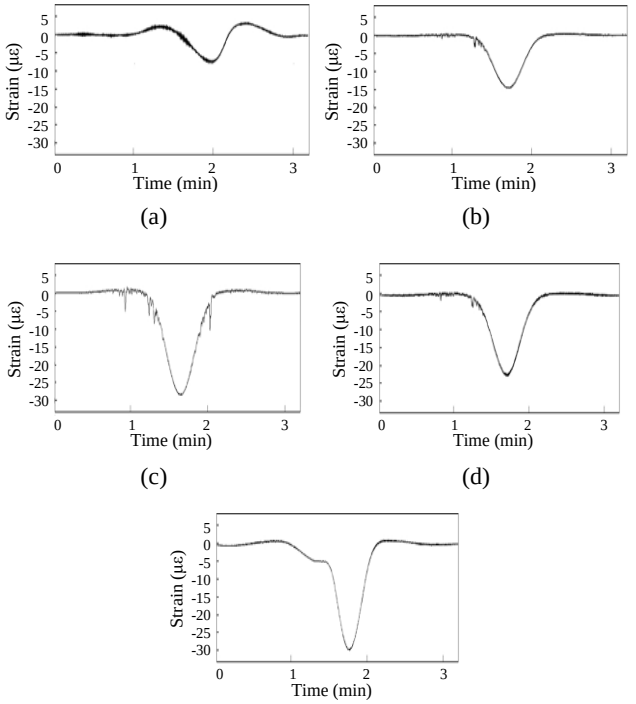

Fig. 6 Measured strains at the vault section (speed = 20 km/h) due to: (a) two trucks running in parallel in the same directions; (b) one train; (c) two trains running in opposite directions; (d) two trucks running in parallelin same directions and two trains running in opposite directions; (e) one train braking

effect of traveling vehicles on the strains at critical locations of the bridge. The impact factor was defined as the percentage of the maximum dynamic strain exceeding the maximum static strain. The static strain was obtained by carrying out a quasi-static test where trains move across the bridge at a crawl speed. Figs. 6(a)-(e) show the measured strain histories at the vault section (E-E) under various vehicle passing scenarios. By comparing Fig. 6(c) with Fig. 6(d), it can be concluded that the impact effect of two trains running in opposite directions is reduced when two trucks run in parallel at the same time. By comparing Fig. 6(b)

with Fig. 6(a), it can be seen that the impact effect of a single train is greater than that of two trucks running in parallel. Overall, train braking has the most significant impact effect on the dynamic response of the bridge as shown in Fig. 6(e). The fundamental code for design on railway bridge and culvert in China (TB 10002.1 2005) recommends that braking force should be taken as ten percent of the vertical static load of the train. Therefore, the calculation of the braking force of a monorail train is 247.2 kN based on the bridge code. The maximum braking force of experiment is 292.9 kN, which is obviously larger than the calculated values based on the specification. The reason may be that the friction coefficient of the rubber tires used by monorail train is greater than that of traditional train tires.

Figs. 7(a)-(d) show the effects of loading scenarios and vehicle speeds on the impact factors based on the strains measured at A-A, B-B, C-C, D-D and E-E sections. Overall, the impact factors at A-A, B-B, and C-C sections are smaller and less sensitive to the speed of vehicles than those at D-D and E-E sections. That is, the impact effect of vehicles on the arch is stronger than that on the girder. It can be seen from Figs. 7(a)-(c) that the peak impact factor of the arch section appears at a speed of 40 km/h when two trucks passes over the bridge in the same direction and 10 km/h when two trains travels through the bridge in opposite directions, while the impact factor curve of the main girder sections has almost no fluctuation at all speed. It may be that the main girder is relatively separated from the main arch, so the two structures can have independent vibration that does not affect each other. Meanwhile, the arch structure may have resonance when the loading frequency is close to the natural frequency of the arch structure at specific speeds. However, the natural frequency of the bridge (0.310 Hz) is quite different from the natural frequency of the train (0.893 Hz), which shows that the resonance is not only determined by the frequency of the vehicle and bridge, but also related to the factors such as the road surface roughness and the vehicle speed. By comparing Fig. 7(a) with Fig. 7(c), the presence of two trains significantly changed the impact effects at D-D and E-E sections. However, by comparing Fig. 7(b) with Fig. 7(c), the presence of two trains had marginal effects on the peak impact factors at D-D and E-E sections. Therefore, the dynamic responses of the bridge were dominated by passing monorail trains rather than the trucks. The reason can be that the quality of the train is far greater than the quality of the truck, so the influence of the truck vibration on the bridge vibration is negligible compared to the train vibration. Fig. 7(d) shows that truck bouncing had most significant impact effect on the bridge. The impact factor was greater than that of the other driving conditions. The most unfavorable speed of bouncing truck, which leads to the greatest impact factor, was 15 km/h. The maximum impact factor was approximately 0.34, which appeared at the arch foot section.

According to the fundamental code for design on railway bridge and culvert in China (TB 10002.1 2005), the impact factor of the arch bridge can be calculated by the eq. (6)

$$IM = \frac{15}{100+\lambda}\left(1+\frac{0.4L}{f}\right) \tag{6}$$

where λ denotes the calculation span of the arch bridge; L denotes the span of the bridge; and f denotes the sagittal height of arch bridge. The impact factor obtained according to the specification is 0.24.

The maximum impact factors of the bridge under the first three loading conditions (two trucks running in parallel in the same directions, two trains running in opposite directions, two trucks running in parallel in the same directions and two trains running in opposite direction) are

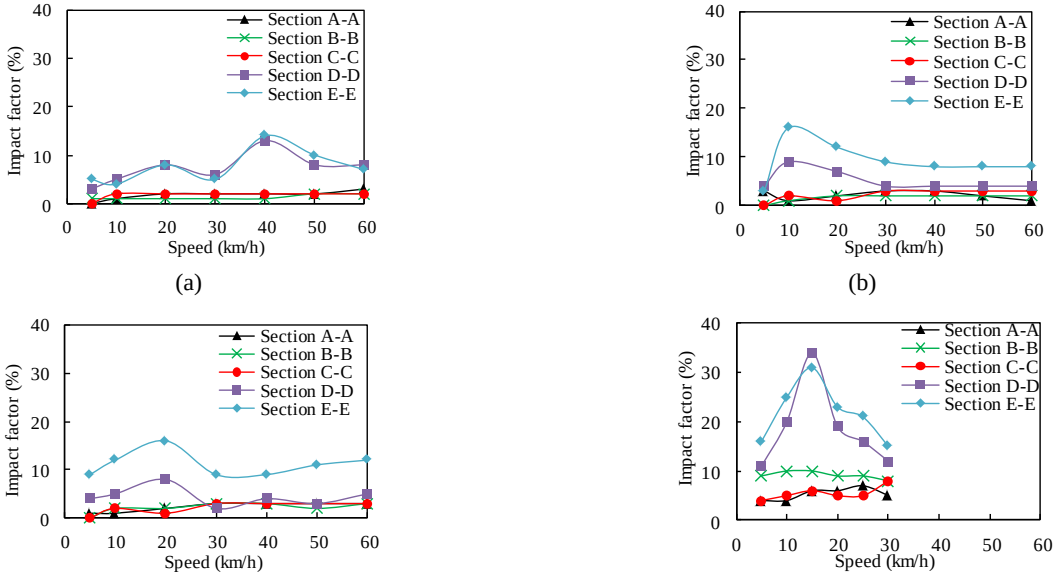

Fig. 7 Impact factors of the bridge under: (a) two trucks running in parallel in the same directions; (b) two trains running in opposite directions; (c) two trucks running in parallel in the same directions and two trains running in opposite directions; (d) truck bouncing

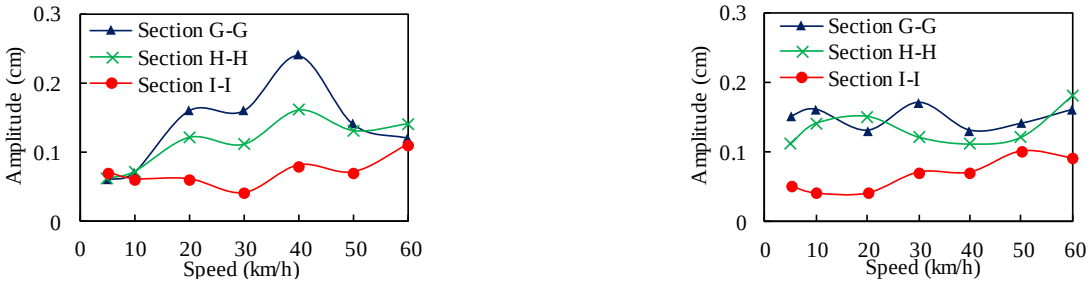

(a) One train running (b) Two trains running

Fig. 8 Measured peak displacement at the bottom chord

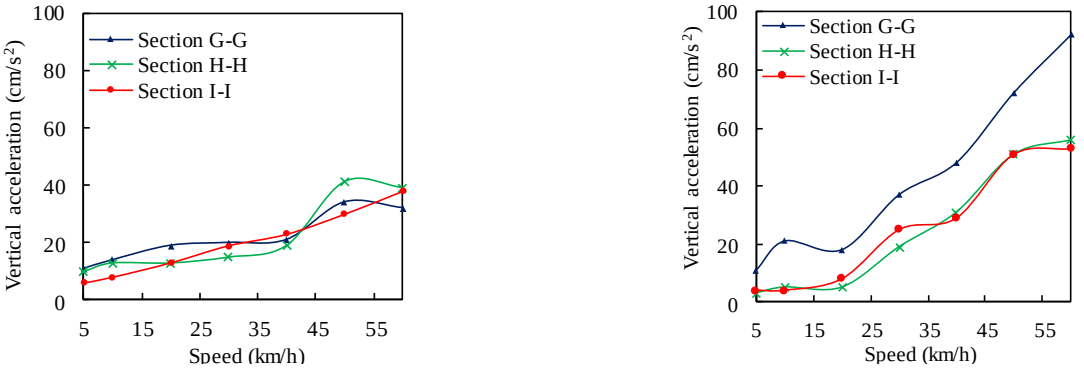

(a) Under one train (b) Under two trains

Fig. 9 Measured peak acceleration of the bridge

0.14, 0.17, 0.16, respectively. They did not exceed 0.24 obtained by the specification, which shows that the impact effect of the moving monorail train on the bridge is not strong. However, truck bouncing produces an impact factor of 0.34 which exceeds the standard value. It shows that the road surface roughness has a great influence on the dynamic response of the vehicle-bridge system. The irregularity of the pavement can greatly aggravate the impact effect of the vehicle on the bridge structure.

4.3 Displacement

When one train and two trains move across the bridge, the peak displacements at three sections are presented in Figs. 8(a) and (b), respectively. Under the excitation of one train, the peak displacement at Section G-G reached its maximum (0.24 cm) at a speed of 40 km/h, as shown in Fig. 8(a). Excited by two trains, the peak displacements did not change significantly with the train speed, and did not necessarily exceed the peak displacements at particular sections induced by one train. This could be attributed to the greater torsion caused by a single train than that by two trains, because the traveling paths of two trains are symmetrical with the centerline of the bridge, thus reducing the torsional effect.

4.4 Acceleration

Fig. 9 shows the measured peak accelerations of the bridge under running trains. As the speed of train was increased from 5 to 60 km/h, the peak vertical and transverse accelerations approximately linearly increased with the speed. Under the same condition, the peak vertical and transverse accelerations are close at each of the three investigated sections. When one train passed through the bridge, the peak vertical and transverse accelerations at different locations of the bridge were about the same. When two trains ran over the bridge, the peak vertical and transverse accelerations at Section G-G are about twice as much as the accelerations at Sections H-H and I-I. It shows that the acceleration response of the middle cross section of the bridge is very sensitive to the number of loaded vehicles, and it presents a doubling increase trend with the increase of the number of loaded vehicles.

5. Finite element analysis

Numerical simulations were performed to understand the dynamic behaviors of the bridge under moving train(s). Finite element models of the bridge and the train subsystems were established, respectively, and then assembled through the train-bridge contact condition. Track irregularity was also taken into consideration in the finite element model.

5.1 Bridge model

Fig. 10 shows the finite element model of the bridge using ANSYS software. The arch, transverse bracings, steel truss girder, Y-shaped rigid frame, and piers were modeled

Fig. 10 Finite element model of the bridge

Table 2 Material properties

Components	Young's modulus (MPa)	Poisson ratio	Unit weight (kN/m^3)
Main arch	2.06×10^5	0.3	78.50
Steel truss girder	2.06×10^5	0.3	78.50
Y-shaped rigid frame	3.60×10^4	0.2	26.00
Main pier	3.45×10^4	0.2	26.00
Abutment pier	3.25×10^4	0.2	25.00
Suspenders and tied bars	1.95×10^5	0.3	78.50
Foundation	3.00×10^4	0.2	25.00

using three-dimensional two-node beam elements; the suspenders and tied bars were modeled using three-dimensional two-node truss elements. A total of 6,515 elements, including 136 truss elements and 6,319 beam elements, were used. The bottom surfaces of the piers were fixed. Linear elastic material properties were adopted, as listed in Table 2.

The equations of motion of the bridge subsystem can be expressed into

$$[\mathbf{M_b}]\{\ddot{\mathbf{X}}_\mathbf{b}\}+[\mathbf{C_b}]\{\dot{\mathbf{X}}_\mathbf{b}\}+[\mathbf{K_b}]\{\mathbf{X_b}\}=\{\mathbf{P_{bv}}\} \quad (7)$$

where $\{\ddot{X}_b\}$, $\{\dot{X}_b\}$ and $\{X_b\}$ represent the nodal acceleration, velocity, and displacement vectors of the bridge; $[C_b]$, $[M_b]$ and $[K_b]$ are the damping, mass, and stiffness matrices of the bridge, respectively; $\{P_{bv}\}$ is the external force vector due to a moving train. In this study, Rayleigh damping was adopted in the finite element model (Shibeshi and Roth 2016). The damping ratio of 0.5% is adopted to calculate the Rayleigh damping which is well in accordance with the obtained from the measured signals.

5.2 Monorail train model

A monorail train is composed of body, bogie, traveling wheel, steering wheel, stabilizing wheel, suspension system, and shock absorber. The traveling wheel is in contact with the bogie from the underside while the steering wheel and stabilizing wheel are engaged with the bogie on two sides. The following four assumptions are employed in the modeling of monorail train:

(1) The train body and bogies are rigid.
(2) The train travels across the bridge at constant speed.
(3) The effect of vertical loads on the stiffness of the traveling wheel is neglected.

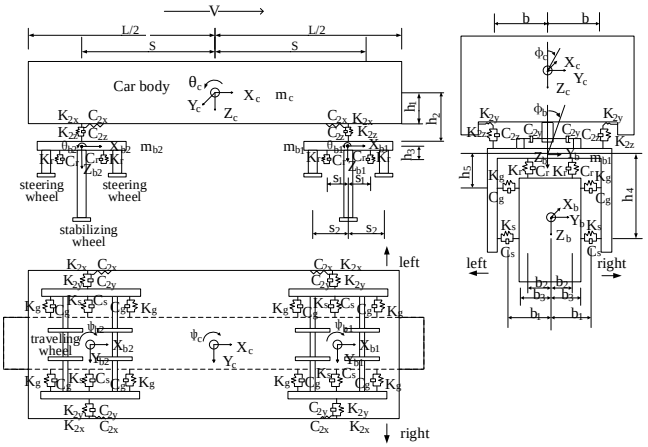

Fig. 11 A 15-DOF model of monorail train

(4) The wheels of a train remain in contact with the bridge deck.

Fig. 11 shows an idealized model of a monorail train with 15 DOFs. Yawing, vertical settlement, side-rolling, head shaking and nodding motions of the body and each bogie are incorporated into this model. The symbols *X*, *Y*, *Z*, and θ indicate the longitudinal, transverse, vertical and rotational displacements, respectively, in the Cartesian coordinate system. Table 3 lists the detailed mechanical and geometric parameters of the monorail train, Mc1, which were provided by the manufacturer of the train.

The equation of motion of the train can be written as

$$[\mathbf{M_v}]\{\ddot{\mathbf{X}}_\mathbf{v}\}+[\mathbf{C_v}]\{\dot{\mathbf{X}}_\mathbf{v}\}+[\mathbf{K_v}]\{\mathbf{X_v}\}=\{\mathbf{P_g}\}+\{\mathbf{P_{vb}}\} \quad (8)$$

where *v* means a vehicle or monorail train; $\{P_g\}$ denotes the gravity force vector of the vehicle; and $\{P_{vb}\}$ denotes the external force applied on the vehicle through the bridge.

5.3 Track irregularity

Track irregularity can significantly affect the dynamic responses of the bridge and vehicles (Liu *et al*. 2009, 2011). It is measured by the deflection of the track beam under the monorail train with its wavelength equal to the internode length of the truss. In the finite element analysis, the track irregularity was represented by a power spectral density function as given in Eq. (9)

$$S(\Omega)=\frac{\alpha}{\Omega^n+\beta^n} \quad (9)$$

where *S* denotes the spectral density function of track irregularity; Ω denotes the spatial frequency (cycle /m); α, β and *n* are the parameters that represent the shape of the spectral density function. The parameters α, β and *n* of the track beam are respectively equal to 0.005, 0.35 and 3.00 under traveling wheel; 0.0006, 0.5 and 2.80 under steering wheel; and 0.0006, 0.5 and 2.60 under stabilizing wheel.

The random track irregularity can be generated from the power spectrum density by

Table 3 Major parameters of the monorail train Mc1 model

Parameters	Value	Unit
Mass of bogie (m_b)	6,170	Kg
Moment of inertia of the bogie on the X axis (I_{xb})	2,850	kg m^2
Moment of inertia of the bogie on the Y axis (I_{yb})	4,650	kg m^2
Moment of inertia of the bogie on the Z axis (I_{zb})	6,550	kg m^2
Mass of train body (m_c)	28,800	Kg
Moment of inertia of the train body on the X axis (I_{xc})	53,900	kg m^2
Moment of inertia of the train body on the Y axis (I_{yc})	539,000	kg m^2
Moment of inertia of the train body on the Z axis (I_{zc})	530,000	kg m^2
Stiffness of traveling wheel (K_r)	1,180	kN/m
Stiffness of steering wheel (K_g)	980	kN/m
Stiffness of stabilizing wheel (K_s)	980	kN/m
Damping of traveling wheel (C_r)	26.1	kN s/m
Damping of steering wheel (C_g)	186	kN s/m
Damping of stabilizing wheel (C_s)	186	kN s/m
Longitudinal stiffness of secondary spring (K_{2x})	130	kN/m
Transverse stiffness of secondary spring (K_{2y})	130	kN/m
Vertical stiffness of secondary spring (K_{2z})	160	kN/m
Longitudinal damping of secondary suspension system (C_{2x})	333.6	kN s/m
Transverse damping of secondary suspension system (C_{2y})	333.6	kN s/m
Vertical damping of secondary suspension system (C_{2z})	22.8	kN s/m
Vertical distance between the center of train body and the upper endpoint of secondary spring (h_1)	0.177	M
Transverse distance between the center of train body and the upper endpoint of secondary spring (b)	1.025	M
Longitudinal distance between the center of train body and the upper endpoint of secondary spring (S)	4.8	M
Vertical distance between the center of train body and the lower endpoint of secondary spring (h_2)	0.88	M
Height between the center of bogie and the center of traveling wheel (h_3)	-0.221	M
Transverse distance between the center of bogie and the center of traveling wheel (b_2)	0.2	M
Longitudinal distance between the center of bogie and the center of traveling wheel (S_1)	0.75	M
Height between the center of bogie and the center of steering wheel (h_5)	-0.061	M
Transverse distance between the center of bogie and the center of steering wheel (b_1)	0.782	m
Longitudinal distance between the center of bogie and the center of steering wheel (S_2)	1.2	m
Height between the center of bogie and the center of stabilizing wheel (h_4)	1.025	m

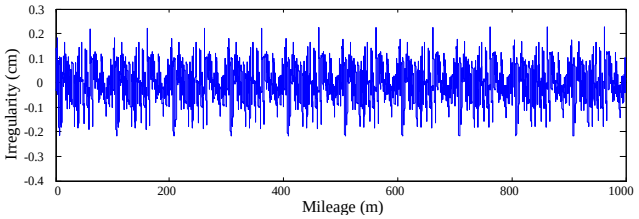

Fig. 12 Sample track irregularity of the track beam at the traveling wheel

$$y(x)=\sum_i \sqrt{2S(\Omega_i)\Delta\Omega}\cdot\cos(2\pi\Omega_i x+\varphi_i) \tag{10}$$

where x, Ω_i, and $\Delta\Omega$ indicate the location in which the track irregularity is generated, frequency component, and frequency increment, respectively; and φ_i represents a random phase angle which is distributed uniformly between 0 to 2π. The upper and lower spatial frequencies Ω_i are 7 m^{-1} and 0.01 m^{-1}, respectively. The frequency increment is set to 0.001 m^{-1}. The track simulation length is 1000 m. The maximum track irregularity generated under traveling wheel, steering wheel and stabilizing wheel, is 2.5 mm, 2.1 mm and 1.8 mm, respectively. A sample of the track irregularity of the track beam under traveling wheel is presented in Fig. 12.

5.4 Monorail train-bridge interaction

The vehicle system and the bridge system are coupled through the wheel track contact relationship. The geometric compatibility conditions at the contact point between the vehicle and the bridge can be expressed as

$$\boldsymbol{X}_v^i=\boldsymbol{X}_b^i+\boldsymbol{y}_s \tag{11}$$

The static equilibrium conditions for the wheel rail interaction force at the contact point

$$\boldsymbol{P}_{bv}^i=\boldsymbol{P}_{vb}^i \tag{12}$$

where i denotes the i_{th} contact point; $\boldsymbol{y}_s$ denotes the displacement vector caused by the track irregularity; $\boldsymbol{P}_{bv}^i$ denotes the force of the train acting on the bridge; $\boldsymbol{P}_{vb}^i$ denotes the force of the bridge acting on the train.

The motion Eqs. (7) and (8) of the train and the bridge can be integrated through the control Eqs. (11) and (12), and the motion equation of the coupled train-bridge system

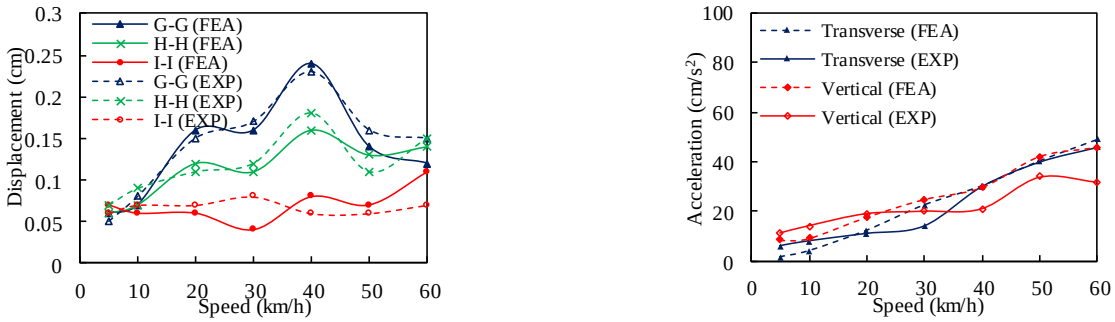

(a) Peak displacement (b) Peak acceleration

Fig. 13 Comparison of experimental and numerical results when one train travels through the bridge

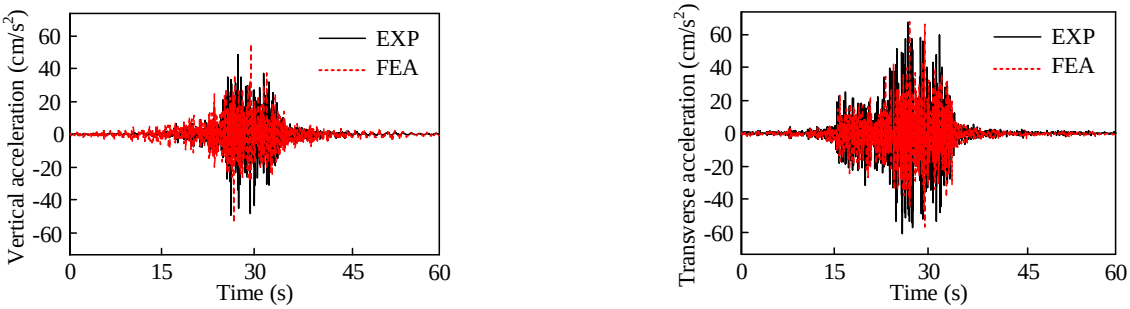

(a) Vertical acceleration (b) Transverse acceleration

Fig. 14 Comparison of experimental and numerical results of the time history accelerations at mid-span section of the bridge under a train running at 60 km/h

can be written as

$$\begin{bmatrix}\mathbf{M}_b & \mathbf{0}\\ \mathbf{0} & \mathbf{M}_v\end{bmatrix}\begin{bmatrix}\ddot{\mathbf{X}}_b\\ \ddot{\mathbf{X}}_v\end{bmatrix}+\begin{bmatrix}\mathbf{C}_b & \mathbf{C}_{bv}\\ \mathbf{C}_{vb} & \mathbf{C}_v\end{bmatrix}\begin{bmatrix}\dot{\mathbf{X}}_b\\ \dot{\mathbf{X}}_v\end{bmatrix}+\begin{bmatrix}\mathbf{K}_b & \mathbf{K}_{bv}\\ \mathbf{K}_{vb} & \mathbf{K}_v\end{bmatrix}\begin{bmatrix}\mathbf{X}_b\\ \mathbf{X}_v\end{bmatrix}=\begin{bmatrix}\mathbf{P}_b\\ \mathbf{P}_v\end{bmatrix} \quad (13)$$

where **M**, **C** and **K** indicate the mass, damping and stiffness matrices, respectively; and **P** is the force vector. Subscripts *b*, *v*, *bv* (or *vb*) denote the bridge, vehicle (train), and vehicle-bridge interaction, respectively. The solution of the dynamic response of the train-bridge system is achieved by the self-compiled program in Fortran language. The motion equations of the train-bridge interaction are solved by the Newmark-β integral method (Guo et al. 2001). The calculation parameters in the method, γ and β, are 0.5 and 0.25, respectively. The time step Δt is set to 0.001s.

5.5 Model validation

The numerical vibration frequencies of the bridge are compared with the experimentally measured values in Table 1. The maximum error in frequency prediction from the finite element model was 3.5%.

Fig. 13(a) compares the experimental and numerical displacements of the bridge at various sections. Overall, the numerical results are in good agreement with the measured displacements. The numerical and experimental accelerations of the track beam in the middle of main span under one train are compared in Fig. 13(b). Overall, the calculated results agree well with their corresponding experimental results in the range of speed from 5 to 60 km/h. The time history acceleration response obtained by field test and numerical analysis is compared in Fig. 14. The experimental and numerical accelerations response in vertical and transverse direction agree reasonably with both the time history curve shape and the peak values. The relative error between the test value and the numerical value is not more than 5%. The discrepancy might be due to assumptions of the numerical model. For example, in the model, it is assumed that the wheel and the track are always in contact, but when the speed of the train is faster or the train is bumping, the wheel may leave the track temporarily. The accuracy of the boundary condition simulation of the bridge model will also cause the error of the calculation results. In addition, when determining the coefficients of Rayleigh damping, if the selected reference frequency w_j is not large enough, it will miss the contribution of some high frequency components of external loads to the dynamic response of the system, which will cause the dynamic response of the system to be smaller than the actual maximum dynamic response. However, the difference between the numerical results and the experimental results is really small, the numerical model is considered to have been validated.

6. Numerical results and discussion

6.1 Deflection

Deflections were calculated at the track beam, joint along the bottom chord, joint along the top chord and the

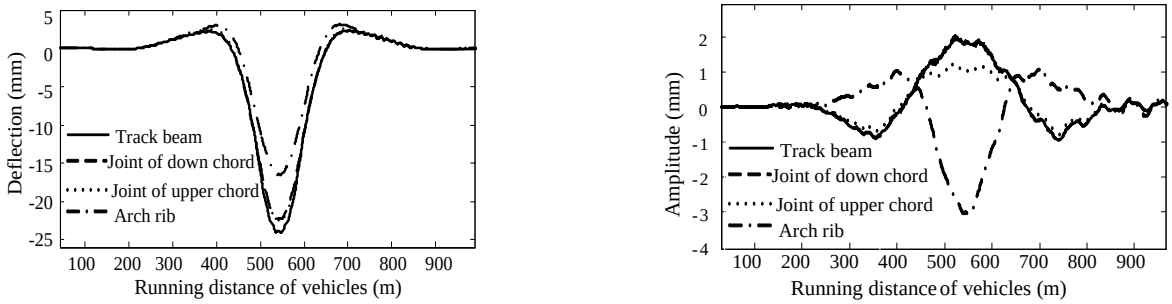

(a) Deflection (b) Transverse displacement

Fig. 15 Time history displacements calculated at mid-span section of the bridge under a monorail train running on a single line at 60 km/h

(a) (b)

Fig. 16 Calculated deflection of the track beam due to: (a) one train; (b) two trains running in opposite directions

arch at each measurement section. Fig. 15 shows the time history displacements calculated at mid-span section of the bridge under a monorail train running on a single line at a speed of 60 km/h. It can be seen from Fig. 15(a) that the maximum and minimum deflections occur in the track beam and the arch rib, respectively. As shown in Fig. 15(b), the maximum transverse displacement occurs in the arch rib. The transverse vibration is mainly caused by the torsional behavior of the bridge so that the arch rib and the truss beam move in opposite directions.

Fig. 16 shows the calculated deflection of the track beam at the middle of main span. The deflection did not change significantly with the change in running speed. The maximum deflection of 4.78 cm occurs at mid-span section with two trains running on the bridge in opposite directions, while the maximum deflection of 2.73 cm occurs at the quarter section of main span with one train running on the bridge. The deflection at the middle of Y-shaped rigid frame remains nearly unchanged under different driving conditions.

6.2 Effect of train braking

The responses of the bridge were analyzed with one train running at 20, 30, and 40 km/h suddenly stops by braking. Figs. 17(a)-(c) show the measured longitudinal displacements of the bridge subjected to one monorail train braking at 40 km/h. There is no significant difference among the longitudinal displacements at various investigated locations of the bridge.

Figs. 18(a)-(c) show the measured longitudinal accelerations of the girder. When the train suddenly stopped by braking, there was a significant difference among longitudinal accelerations at each section. The dynamic

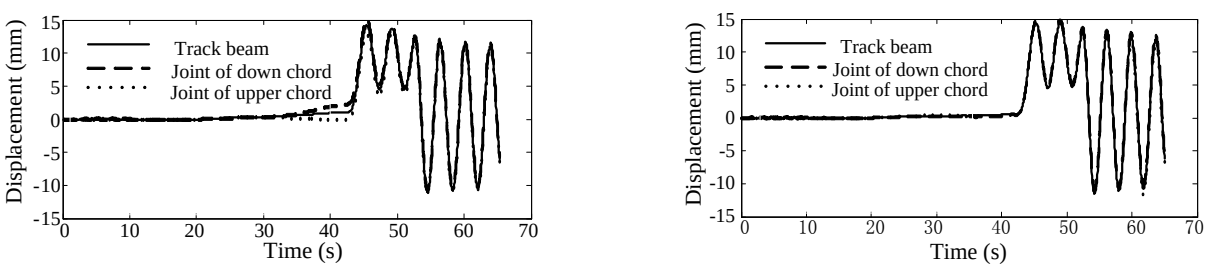

(a) (b)

Fig. 17 The measured longitudinal displacements of the bridge under one monorail train braking at 40 km/h: (a) Section G-G (middle section of main span); (b) Section H-H (quarter section of main span); (c) Section I-I (middle section of Y-shaped rigid frame)

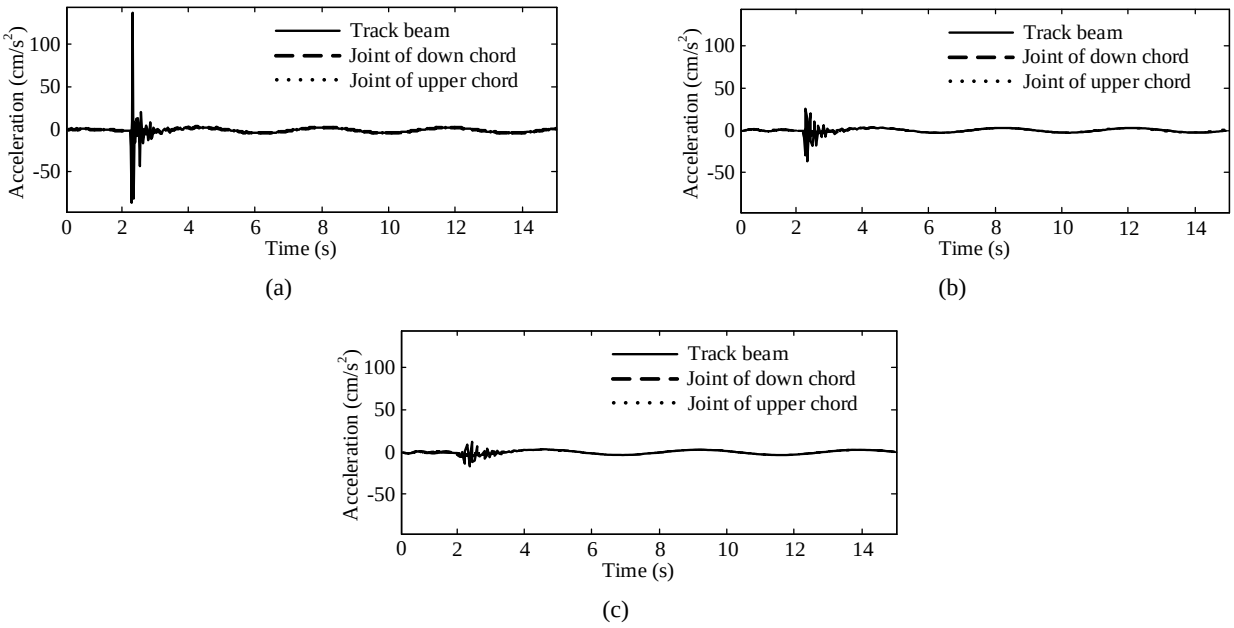

Fig. 18 Longitudinal accelerations under one monorail train braking at 40 km/h: (a) Section G-G (middle section of main span); (b) Section H-H (quarter section of main span); (c) Section I-I (middle section of Y-shaped rigid frame)

effect of braking is the greatest to the areas near the train and attenuates over distance.

7. Evaluation of riding comfort

The running stability of trains is typically evaluated using the Sperling index W_z (Graa *et al*. 2017), which can be expressed into

$$W_Z = 0.896 \cdot \sqrt[10]{\frac{a^3}{f} F(f)} \tag{14}$$

where a denotes the acceleration (cm/s^2); f denotes the vibration frequency (Hz); $F(f)$ represents the correction coefficient related to f. For vertical vibration, $F(f) = 0.325 f^2$ when 0.5 Hz < f < 5.9 Hz; $F(f) = 400 / f^2$ when 5.9 Hz < f < 20 Hz; and $F(f) = 1$ when f > 20 Hz. For transverse vibration, $F(f) = 0.8 f^2$ when 0.5 Hz < f < 5.4 Hz; $F(f) = 650 / f^2$ when 5.4 Hz < f < 26 Hz; and $F(f) = 1$ when f > 26 Hz.

Eq. (14) is applicable to harmonic vibration. However, the vibration induced by a vehicle includes multiple frequency components. Therefore, the measured vibration needs to be decomposed to a series of components at various frequencies (as listed in Table 4). For each of the vibration components, a Sperling index Wzi (i = 1, 2, ... , n) is determined. Finally, an overall Sperling index can be defined as (GB 5599-85 1985)

$$W_z = \sqrt[10]{W_{z1}^{10} + W_{z2}^{10} + \cdots + W_{zn}^{10}} \tag{15}$$

Fig. 19 compares the numerical with experimental maximum accelerations of a train passing through the bridge. Overall, the numerical results agree well with the experimental results. The maximum acceleration in the

Table 4 Natural frequencies of monorail train

Mode	Natural frequency (Hz)
Bouncing: f_1	1.196
Axle hop (front): f_2	5.854
Axle hop (rear): f_3	5.854
Sway: f_4	0.893
Bogie sway (front): f_5	3.987
Bogie sway (rear): f_6	3.987
Rolling: f_7	1.598
Axle tramp (front): f_8	4.531
Axle tramp (rear): f_9	4.531
Pitching: f_{10}	1.685
Bogie windup (front): f_{11}	4.352
Bogie windup (rear): f_{12}	4.352
Yawing: f_{13}	2.194
Bogie tramp (front): f_{14}	3.997
Bogie tramp (rear): f_{15}	3.997

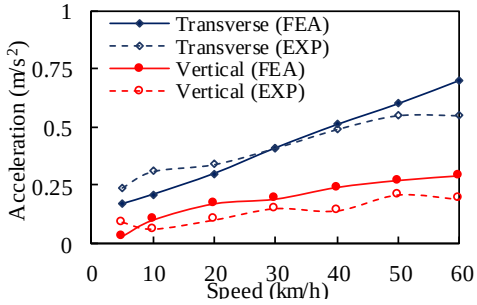

Fig. 19 Numerical versus experimental maximum accelerations of a train passing through the bridge

Table 5 Evaluation criteria of Sperling index

Sperling index W_z	Riding comfort	Sperling index W_z	Riding quality
1	Slightly felt	1	Excellent
2	Obviously felt	2	Good
2.5	More obviously felt but still comfortable	3	Meet the requirement
3	Strong and abnormal but tolerable	4	Allow operation
3.25	Extremely abnormal	4.5	Not allowed to run
3.5	Extremely abnormal and not endurable for long	5	Dangerous
4	Very uncomfortable and harmful to stand for long	/	/

Table 6 Running stability grade of the vehicle in China

Running stability grade Evaluation level		Sperling index	
		Passenger train	Freight train
Class 1	Excellent	< 2.5	< 3.5
Class 2	Good	2.5–2.75	3.5–4.0
Class 3	Qualified	2.75–3	4.0–4.25

transverse direction is greater than that in the vertical direction. As the train speeded up from 5 to 60 km/h, the maximum acceleration increased with the speed particularly in the transverse direction.

Table 5 lists the correlation between the Sperling index and the riding comfort and between the Sperling index and the category of riding quality (Graa *et al*. 2017). Table 6 lists the running stability grade of the vehicle specified in China code (GB 5599-85 1985).

Fig. 20 presents the riding comfort index as a function of running speed. It can be clearly seen from Fig. 20 that the comfort index remains nearly the same as one or two trains pass through the bridge. With the increase of running speed, the acceleration and Sperling index of the train increase, and the riding comfort level decreases. Since the vertical acceleration of the train is much smaller than the transverse acceleration, the vertical comfort level is higher than the transverse comfort level. The running speed is a control factor for riding comfort.

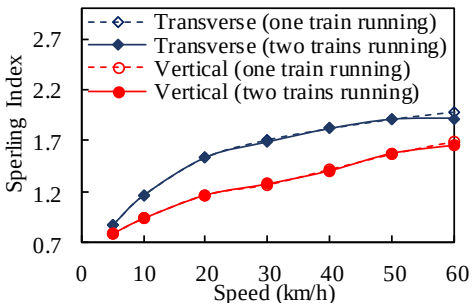

Fig. 20 Comfort index of monorail trains

When the vertical and transverse accelerations of a vehicle are less than 2.45 m/s^2 and 1.47 m/s^2, respectively, the riding comfort of the vehicle is considered to be excellent according to the MOR Standard (TB/T-2360-93 1993). For the bridge under investigation, the maximum transverse and maximum vertical accelerations of the train are 0.59 m/s^2 and 0.22 m/s^2, both less than the acceleration limit for excellent riding comfort. In fact, Fig. 20 indicates that the comfort index of the train is mostly between 1 (slightly felt) and 2 (obviously felt). According to the railway code (GB 5599-85 1985) for evaluating the running stability of the train, the grade of the train running stability is excellent.

8. Conclusions

Based on the experimental and numerical studies, the following conclusions can be drawn:

- The strains in arch rib of the bridge were greater than those in bridge girder. The stiffness of arch out-plane is smaller than that of in-plane. The impact factor of truck bouncing was 0.34 at the most unfavorable truck speed of 15 km/h, which shows that the poor road surface roughness can greatly aggravate the impact effect of the vehicle on the bridge structure. A resonance may occur when trucks running at 40 km/h or trains running at 20 km/h.
- Regardless of the running speed of a train, the transverse vibration of the bridge was mainly caused by the torsional motion of the bridge when the arch rib and the truss girder vibrated out of phase. The maximum transverse displacement of 0.24 cm occurred at the middle section of main span when one train ran across the bridge at a speed of 40 km/h. Two trains running in opposite direction reduced the transverse displacement of the bridge.
- The vertical and transverse accelerations of the bridge were close, both increasing with the running speed of vehicle. The maximum transverse acceleration of 89 cm/s^2 occurred at the middle span when two trains ran on the bridge in the opposite direction. The acceleration response of the middle section of the bridge is very sensitive to the number of loaded vehicles, and it presents a doubling increase trend with the increase of the number of loaded vehicles.
- The acceleration of the train changed little when it encountered another train passing by the bridge. It increased with the running speed of the train. The transverse acceleration of the train exceeded the vertical acceleration, thus less riding comfort in transverse direction. The running speed instead of the number of trains determined the riding comfort of a train. The maximum transverse acceleration of the car body was 0.59 m/s^2.
- The sudden braking of a train has the maximum impact on the longitudinal acceleration of nearby sections of the steel truss girder, which attenuates

over distance. The maximum longitudinal acceleration of 138.55 cm/s^2 occurred at the middle of main span when one train suddenly braked at a speed of 40 km/h.

- Although the natural frequency of the bridge (0.310 Hz) is quite different from the natural frequency of the train (0.893 Hz), the dynamic response of the bridge still has a peak value at lower speed, which shows that the resonance of monorail bridge is also sensitive to other factors such as road surface roughness and driving speed, instead of the frequency alone. The vertical deformation of the arch is less than that of the girder, while the lateral deformation is much larger than that of the girder. Therefore, it is necessary to verify the out-plane stiffness of the arch in the design. The dynamic response of the middle section of the main span is much more sensitive to the number of loaded monorail trains compared to the other cross sections (such as the middle section of the side span and the middle section of the Y frame). When the two monorail trains are on the bridge at the same time, it is suggested that the speed of the train is not more than 60 km/h. No more than 0.2 for the designed impact factor according to the experimental results.
- The numerical displacement and acceleration of the bridge were in good agreement with their corresponding responses. Therefore, the proposed finite element model can be used for other similar types of bridges in a cost-effective way.

Acknowledgments

This study was supported in part by the National Natural Science Foundation of China [grant No. 51108382 and 51508474], and by the Science and Technology Research and Development Plan of China Railway Construction [grant No. 2014-C34]. Scholarship for the first author to visit Missouri University of Science and Technology was made possible by the Chinese Scholarship Council [grant No. P-1-02556].

References

Altunisik, A.C. and Kalkan, E. (2016), "Investigation of earthquake angle effect on the seismic performance of steel bridges", *Steel Compos. Struct., Int. J.*, **22**(4), 855-874.

Androus, A., Afefy, H.M. and Sennah, K. (2017), "Investigation of free vibration and ultimate behavior of composite twin-box girder bridges", *J. Constr. Steel Res.*, **130**, 177-192.

Ataei, S., Tajalli, M. and Miri, A. (2016), "Assessment of load carrying capacity and fatigue life expectancy of a monumental Masonry Arch Bridge by field load testing: A case study of veresk", *Struct. Eng. Mech., Int. J.*, **59**(4), 703-718.

Cavdar, O. (2013), "Probabilistic sensitivity analysis of suspension bridges to near-fault ground motion", *Steel Compos. Struct., Int. J.*, **15**(1), 15-39.

Deng, J., Liu, A., Yu, Q. and Peng, G. (2016), "Seismic performances of steel reinforced concrete bridge piers", *Steel Compos. Struct., Int. J.*, **21**(3), 661-677.

Dinh, V.N., Kim, K.D. and Warnitchai, P. (2009), "Dynamic analysis of three-dimensional bridge-high-speed train interactions using a wheel-rail contact model", *Eng. Struct.*, **31**(12), 3090-3106.

GB 5599-85 (1985), Railway Vehicles-Specification for Evaluation the Dynamic Performance and Accreditation Test, National Bureau of Standards; Beijing, China. [In Chinese]

Goda, K., Nishigaito, T., Hiraishi, M. and Iwasaki, K. (2000), "A curving simulation for a monorail car", *Railroad Conference*, 171-177.

Gou, H.Y., Shi, X.Y., Zhou, W., Cui, K. and Pu, Q.H. (2017), "Dynamic performance of continuous railway bridges: Numerical analyses and field tests", *Proceedings of the Institution of Mechanical Engineers, Part F: Journal of Rail and Rapid Transit*. DOI: 10.1177/0954409717702019

Gou, H.Y., Long, H., Bao, Y., Chen, G., Pu, Q.H. and Kang, R. (2018a), "Experimental and numerical studies on stress distributions in girder-arch-pier connections of long-span continuous rigid frame arch railway bridge", *J. Bridge Eng.* [In Press]

Gou, H.Y., Wang, W. and Shi, X.Y. (2018b), "Behavior of steel-concrete composite cable anchorage system", *Steel Compos. Struct.*, **26**(1), 115-123.

Gou, H.Y., Long, H., Bao, Y., Chen, G. and Pu, Q.H. (2018c), "Dynamic behavior of hybrid framed arch railway bridge under moving trains", *Steel Compos. Struct., Int. J.*, [Under Review]

Gou, H.Y., He, Y.N., Zhou, W., Bao, Y. and Chen, G. (2018d), "Experimental and numerical investigations of the dynamic responses of an asymmetrical arch railway bridge", *P I MECH ENG F-J RAI*.

Graa, M., Nejlaoui, M., Houidi, A., Affi, Z. and Romdhane, L. (2017), "Modeling and simulation for lateral rail vehicle dynamic vibration with comfort evaluation", *Adv. Acoust. Vib.*, **5**, 89-100.

Guo, W.H. and Xu, Y.L. (2001), "Fully computerized approach to study cable-stayed bridge-vehicle interaction", *J. Sound Vib.*, **248**(4), 745-761.

Gűnaydin, M., Adanur, S., Altunişik, A.C., Sevı, B. and Tűrker, E. (2014), "Determination of structural behavior of Bosporus suspension bridge considering construction stages and different soil conditions", *Steel Compos. Struct., Int. J.*, **17**(4), 1229-9367.

Hogan, L.S., Wotherspoon, L., Beskhyroun, S. and Ingham, J. (2016), "Dynamic field testing of a three-span precast-concrete bridge", *J. Bridge Eng.*, **21**(12), 06016007.

Jiang, D.Q., Terzioglu, T., Hueste, M.B.D., Mander, J.B. and Fry, G.T. (2016), "Experimental study of an in-service spread slab beam bridge", *Eng. Struct.*, **127**, 525-535.

Jorquera-Lucerga, J.J., Lozano-Galant, J.A. and Turmo, J. (2016), "Structural behavior of non-symmetrical steel cable-stayed bridges", *Steel Compos. Struct., Int. J.*, **20**(2), 447-468.

Kashani, H. and Nobari, A.S. (2012), "Structural Nonlinearity Identification Using Perturbed Eigen Problem and ITD Modal Analysis Method", *Appl. Mech. Mater.*, **232**, 949-954.

Kwon, S.D., Lee, J.S., Moon, J.W. and Kim, M.Y. (2008), "Dynamic interaction analysis of urban transit maglev vehicle and guideway suspension bridge subjected to gusty wind", *Eng. Struct.*, **30**(12), 3445-3456.

Lee, C.H., Kim, C.W., Kawatani, M., Nishimura, N. and Kamizono, T. (2005), "Dynamic response analysis of monorail bridges under moving trains and riding comfort of trains", *Eng. Struct.*, **27**(14), 1999-2013.

Lee, C.H., Kawatani, M. and Kim, C.W. (2006), "Dynamic response of a monorail steel bridge under a moving train", *J. Sound Vib.*, **294**(3), 562-579.

Li, G.Q., Wang, Z.L., Chen, S.W. and Xu, Y.L. (2016a), "Field measurements and analyses of environmental vibrations induced

by high-speed Maglev", *Sci. Total Environ.*, **568**, 1295-1307.
Li, Y., Cai, C.S., Liu, Y., Chen, Y.J. and Liu, J.F. (2016b), "Dynamic analysis of a large span specially shaped hybrid girder bridge with concrete-filled steel tube arches", *Eng. Struct.*, **106**, 243-260.
Liu, Z., Luo, S., Ma, W. and Song, R. (2009), "Application research of track irregularity PSD in the high-speed train dynamic simulation", *Proceedings of International Conference on Transportation Engineering*, Chengdu, China, July.
Liu, X., Lian, S. and Yang, W. (2011), "Influence analysis of irregularities on vehicle dynamic response on curved track of speed-up railway", *Proceedings of International Conference on Transportation Engineering*, Chengdu, China, July.
Madrazo-Aguirre, F., Ruiz-Teran, A.M. and Wadee, A. (2015), "Dynamic behavior of steel-concrete composite under-deck cable-stayed bridges under the action of moving loads", *Eng. Struct.*, **103**, 260-274.
Mellat, P., Andersson, A., Pettersson, L. and Karoumi, R. (2014), "Dynamic behavior of a short span soil–steel composite bridge for high-speed railways–Field measurements and FE-analysis", *Eng. Struct.*, **69**(9), 49-61.
Shibeshi, R.D. and Roth, C.P. (2016), "Field measurement and dynamic analysis of a steel truss railway bridge", *J. S. Afr. Inst. Civ. Eng.*, **58**(3), 28-36.
Tao, T.Y., Wang, H., He, X.H. and Li, A.Q. (2016), "Evolutionary power spectral density analysis on the wind-induced buffeting responses of Sutong Bridge during Typhoon Haikui", *Adv. Struct. Eng.*, **20**(2), 214-24.
TB 10002.1 (2005), Fundamental code for design on railway bridge and culvert, Chinese Railway Ministry; Beijing, China. [In Chinese]
TB/T-2360-93 (1993), Evaluation Method and Evaluation Standard of Railway Locomotive Dynamic Performance Test, Chinese Railway Ministry; Beijing, China. [In Chinese]
Terzioglu, T., Jiang, D.Q., Hueste, M.B.D., Mander, J.B. and Fry, G.T. (2016), "Experimental investigation of a full-scale spread slab beam bridge", *J. Bridge Eng.*, **21**(11), 04016082.
Toydemir, B., Koçak, A., Sevim, B. and Zengin, B. (2017), "Ambient vibration testing and seismic performance of precast i beam bridges on a high-speed railway line", *Steel Compos. Struct., Int. J.*, **23**(5), 557-570.
Xia, C.Y., Lei, J.Q., Zhang, N., Xia, H. and Roeck, G.D. (2012), "Dynamic analysis of a coupled high-speed train and bridge system subjected to collision load", *J. Sound Vib.*, **331**(10), 2334-2347.
Yang, M.G., Cai, C.S. and Chen, Y. (2015), "Creep performance of concrete-filled steel tubular (CFST) columns and applications to a CFST arch bridge", *Steel Compos. Struct., Int. J.*, **19**(1), 111-129.
Youcef, K., Sabiha, T., Mostafa, D.E., Ali, D. and Bachir, M. (2013), "Dynamic analysis of train-bridge system and riding comfort of trains with rail irregularities", *J. Mech. Sci. Technol.*, **27**(4), 951-962.